Characterization and super-capacitive properties of nanocrystalline copper ferrite prepared via green and chemical methods

M. Khairy [a,b,*], M.G. El-Shaarawy [c], M.A. Mousa [a]

[a] Chemistry Department, Faculty of Science, Benha University, Benha, Egypt
[b] Chemistry Department, College of Science, Imam Mohammad Ibn Saud Islamic University, Riyadh, Saudi Arabia
[c] Physics Department, Faculty of Science, Benha University, Benha, Egypt

ARTICLE INFO

ABSTRACT

A comparison was made between the structure and electrochemical properties of CuFe$_2$O$_4$ nanoparticles prepared by five different preparation methods, involving the co-precipitation, green sol–gel, green hydrothermal, auto-combustion, and microwave. The obtained ferrites were characterized by FT-IR, XRD, BET, SEM, and TEM techniques. A spinel crystal structure was observed for all samples with morphological structures, surface textural properties, and particle sizes hanging on the synthesis process and set in the range of 12–45 nm. The sample prepared in the presence of gelatin shows well-dispersed nanosphere particles. The electrochemical properties of obtained ferrites were studied using cyclic voltammetry, charge–discharge, and electrochemical impedance spectroscopy. The as-synthesized CuFe$_2$O$_4$ (Cu$_{gg}$) sample acts as excellent electrode material in supercapacitor with a high specific capacitance of 145F g^{-1}, an energy density of 18.9 Wh kg^{-1}, and a power density of 486 Wkg^{-1} at 1 Ag^{-1} and good retention value of 90.2% after 1000 cycles at 1Ag^{-1}.

1. Introduction

Ferrite possessing common formula MFe$_2$O$_4$ (M = divalent metal ion, e.g. Zn, Mg, Mn, etc.) is one of the most important materials that can be used for many purposes such as ceramics, pigments, electronic, microwave absorbents, supercapacitors and solid batteries.[1–5] The properties and applications of these materials are highly dependent on the size, shape, and structure, of the particles, which are controlled by the preparation process.[6–10]

There are various physical, chemical, biological, and hybrid methods for the synthesis of ferrite nanoparticles like ceramic method,[7] mechanical alloying,[8] sonochemical technique,[9] solvothermal methods,[10] microwave processing approaches,[11] coprecipitation, [12] sol–gel methods,[13] etc. The ceramic method is time-consuming. It also produces particles of relatively large size because of high-temperature treatment. Chemical synthesis methods have the advantage over the ceramic method because (i) it is carried out at relatively low temperatures, (ii) it produces fine (iii) the method requires less time, (iv) and essentially the product is reproducible. It is important to report that the sol–gel method has definite advantages over other wet chemical methods because the method is simple, cost-effective low processing temperatures, and produces homogeneous fine particles of nanometer dimensions with a narrow size distribution, in relatively short processing time.[14]

Among synthesis techniques, the green synthesis is used to produce ferrite powders from plant extracts. It is superior to various other techniques as it is clean, eco-friendly with low reaction temperature and free from undesirable harmful by-products.[15]

Supercapacitor is a promising device for energy storage applications since it exhibits attracting characteristics such as high power, minimum equivalent series resistance and extreme cycle life.[5,6] Nanomaterials play fundamental responsibility in energy storage devices, especially, supercapacitors and batteries. Electrochemical supercapacitor performance is mainly controlled by various factors such as electrode material surface, morphology, current collector, separator, and electrolyte.[16] Controllably prepared nanomaterials exhibit interesting morphologies, which plays the virtual major role in the electrochemical activities. [17,18]

Ferrite materials demonstrate attractive magnetic, phase transitions and electrical properties with chemical and thermal stabilities.[19,20] The preparation of the ferrite materials in nano size play fundamental responsibility in energy storage devices, especially, supercapacitors and batteries.[21] Electrochemical supercapacitor implementation is essentially controlled by numerous factors such as electrode material

surface, morphology, current collector, separator, and electrolyte.[16]

Most of the properties required for ferrite applications are extrinsic and not intrinsic. Consequently, it is important to study the effects of preparation methods on structural features of cupper ferrite nanoparticles and their physical properties. We reported previously the impact of preparation method on the particle size, magnetic, optical, and catalytic properties of $CuFe_2O_4$.[22] In the present work, we extend our work to study the effect of synthetic tools using green and chemical methods (co-precipitation, green sol–gel, green hydrothermal, autocombustion, and microwave) on the electrochemical properties of $CuFe_2O_4$.

2. Experimental

2.1. 1. Materials

All materials used without further purification. Copper (ll) nitrate $[Cu(NO_3)_2 \cdot 3H_2O]$ was purchased from SD fine chem Limited, Mumbai 400 030. Ferric nitrate $[Fe(NO_3)_3 \cdot 9H_2O]$ was purchased from LOBA CHEMIE PVT.LTD. Gelatin type B was purchased from Sigma-Aldrich, St. Louis. MC, USA, and Hibiscus flower/ leaves from the local market.

2.2. Synthesis of samples

2.2.1. Hibiscus flower extract preparation

The extract was prepared by boiling 10 g of dried flowers in 150 ml distilled water for 20 min. The extract obtained was left to cool at room temperature and filtered.

2.2.2. Self-combustion method

In this method, 2×10^{-3} mol of $Cu(NO_3)_2 \cdot 3H_2O$ and 4×10^{-3} mol of $Fe(NO_3)_3 \cdot 9H_2O$ were put gradually with stirring into the aqueous Hibiscus rosa-Sinensis flower extract. The solution pH was raised to pH = 10 using NaOH aqueous solution. The gel was formed after concentrated on the solution. This gel was put on a heater at 300 °C. The gel started to melt following by decomposition spontaneously by self-ignition to form a voluminous foam. The powder obtained washed carefully with bi-distilled water and then dried in an oven for 24 h.[23] The sample is symbolized as Cu_{gc}.

2.2.3. Green – Hydrothermal method

2×10^{-3} mol of $Fe(NO_3)_3 \cdot 9H_2O$, 1×10^{-3} mol of $Cu(NO_3)_2 \cdot 3H_2O$, and 0.1 g of gelatin were dissolved in 150 ml of distilled water with stirring for 30 min. Then 12 ml of NaOH (1 M) was gradually inserted to get a pH of 10. The obtained mixture was then transferred into a Teflon-lined stainless autoclave and put it in an oven at 180 °C for 7 h. Next, after cooling the autoclave, the acquired precipitates were washed several times with distilled water then dried at room temperature. The obtained precipitate was finally dried for 24 h in an oven.[24] The sample is symbolized as Cu_{gh}.

2.2.4. Co-Precipitation method

100 ml 5 M NaOH solution was added slowly to 150 ml of a mixture of 2.5×10^{-2} mol $Cu(NO_3)_2 \cdot 3H_2O$ and 5×10^{-2} mol $Fe(NO_3)_3 \cdot 9H_2O$ then heated at 85 °C for 1.5 h, filtered, washed with bi-distilled water and dried at 85 °C for 15 h and finally calcined at 700 °C for 5 h. The sample is symbolized as Cu_{co}.

2.2.5. Microwave method

$CuFe_2O_4$ nanoparticles were synthesized using the microwave technique.[25] In a typical experiment, 2×10^{-2} mol of $Fe(NO_3)_3 \cdot 9H_2O$ and 1×10^{-2} mol of $Cu(NO_3)_2 \cdot 3H_2O$ were mixed in 100 ml water. Then, NaOH solution (1 M) was gradually supplemented into the solution until the pH of the mixture was 10 under microwave irradiation 20 min, 600 W (40 s On, 40 s Off). The suspended solution obtained was cooled for 30 min at room temperature. The precipitate obtained was centrifuged

for 20 min at 3,000 rpm, washed with bi-distilled water and ethanol four times. Finally, the precipitate was dried in an oven at 100 °C for 4 h followed by calcination at 700 °C for 5 h.[21] The sample is symbolized as Cu_{mc}.

2.2.6. Green- Sol-Gel Method:-

A mixed powder of 2×10^{-2} mol of $Fe(NO_3)_3 \cdot 9H_2O$, 1×10^{-2} mol of $Cu(NO_3)_2 \cdot 3H_2O$, and 0.1 g gelatin were dissolved in a beaker containing 200 ml of bi- distilled water with slow stirring at a heating temperature of 50 °C for 2 h. The temperature was then increased to ~ 80 °C and kept under stirring to form a gel. The gel was then calcined at 350 °C for 2 h at a heating rate 10 °C/min to eliminate the residual organic matter. The produced powder was calcined for 7 h at 700 °C for 5 h using a heating rate of 5 K/min.[26] The sample is denoted as Cu_{gg}.

2.3. Characterization methods

2.3.1. X-ray diffraction (XRD)

XRD data of the ferrite samples were collected on Philips X' Pert Pro Super diffractometer with Cu Kα radiation (λ = 1.54 Å) in the range of 2θ = 10-80°.

2.3.2. Fourier transform infrared spectra (FT-IR)

The FT-IR spectra of the ferrite samples were verified using a Brucker-FT-IR. The absorbance was automatically registered against wavenumber in the range of 400–4000 cm^{-1}.

2.3.3. Scanning and Transmission Electron Microscope (SEM and TEM):-

Transmission and Scanning Electron Microscope analyses (TEM) and (SEM) were done by using JEOL-2010 and JEOL JEM-100CXII, respectively.

2.3.4. Nitrogen adsorption measurements

The volumetric method was used to measure the adsorption of nitrogen gas at liquid nitrogen temperature. In all cases, the adsorbent surface will be cleared out of adsorbed molecules generally by thermal outgassing before the N_2 physical adsorption isotherm can be determined. The outgassing process of the ferrite samples was performed at 473 K for 2 h.

2.3.5. Electrochemical properties

Electrochemical measurements were performed in a conventional three-electrode system in 1 M LiCl electrolyte at room temperature, using Pt square foil (area = 0.61 cm^2) as a counter electrode, and saturated calomel as a reference electrode. The working electrode was made by mixing 8 mg, 1 mg, and 1 mg of the cupper ferrite sample, acetylene black, and polytetrafluorethylene (5% wt), respectively to get homogeneous slurry. The slurry was coated onto stainless steel and dried at 230 K for 24 h. The cyclic voltammetry (CV) in the range −0.2 to 0.8 V was performed at different scan rates. The galvanostatic charge/discharge (CD) at a different current density) was tested using a CHI660D electrochemical working station (Shanghai, China). Electrochemical Impedance Spectroscopy (EIS) was carried out by using an ac volt amplitude 5 mV between the frequency ranges 0.1 Hz to 100 k Hz.

3. Results and discussion

3.1. X-Ray powder diffraction analysis

The XRD patterns of the investigated $CuFe_2O_4$ samples have been presented in Fig. 1(a-e). All samples show diffraction peaks around angles of 19.0, 31.4, 36.9, 38.9, 44.9, 55.8, 59.4, and 65.2° corresponds to the crystal planes (111), (220), (311), (222), (400), (422), (511), and (440), respectively confirming the construction of a single phase (fcc) spinel structure which is consistent with standard JCPDS data (#23–0283). All samples also exhibited characteristic reflection peaks
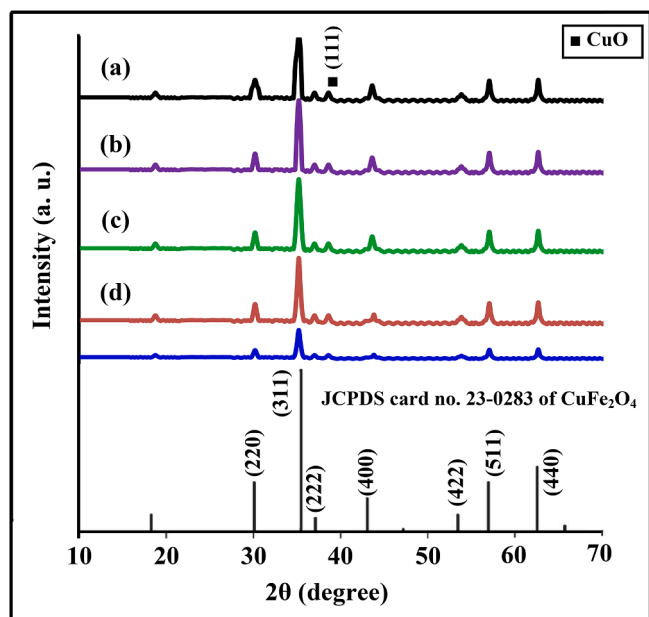
Fig. 1. XRD of the CuFe$_2$O$_4$ samples: (a), Cu$_{mc}$; (b), Cu$_{gh}$; (c), Cu$_{gc}$; (d), Cu$_{co}$ and (e), Cu$_{gg}$.

related to (1 1 1) plane for tenorite (CuO) as a secondary phase besides the main spinel phase of CuFe$_2$O$_4$ crystal. The crystal sizes of nanoparticles were estimated by using the Scherrer equation[27] and found to be 13, 18, 22, 37 and 44 nm for Cu$_{gg}$, Cu$_{co}$, Cu$_{gc}$, Cu$_{gh}$, and Cu$_{mc}$ samples, respectively.

3.2. Fourier transform infrared spectra (FT-IR)

FT- IR spectra of all CuFe$_2$O$_4$ specimens are shown in Fig. 2. The spectra reveal two major transmittance bands at 545–595 cm^{-1} and 410 – 470 cm^{-1}, which are reported to metal oxide stretching vibrations of the octahedral and tetrahedral sites in spinels, respectively.[28] The change in the band positions of the prepared samples is attributed to the change in the Fe^{3+}–O^{2-} and Cu^{2+}–O^{2-} distances by changing the preparation method.[29] The FT-IR spectra also show a peak at ∼ 1640 cm^{-1} and wide-ranging band peak at ∼ 3440.cm^{-1}, which are appointed to the bending and stretching vibration of O–H connected to the

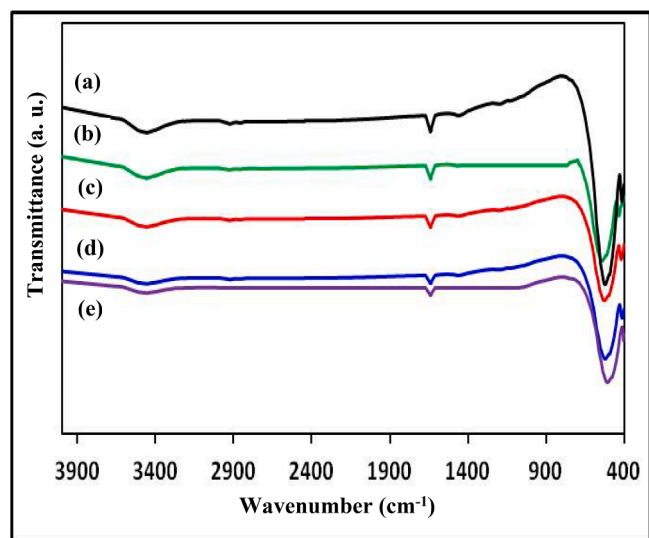**Fig. 2.** FT-IR of CuFe$_2$O$_4$: (a) Cu$_{co}$; (b) Cu$_{mc}$; (c) Cu$_{gh}$; (d) Cu$_{gc}$; (e)Cu$_{gg}$.

adsorbed water.

3.3. SEM and TEM study

Since synthetic conditions highly affect the structural properties of the nanoparticles,[30–33] therefore, microstructure studies on the prepared samples have been carried out by TEM and SEM techniques. Fig. 3 (A, B), reveal SEM and TEM images of the produced CuFe$_2$O$_4$ samples. The samples showed different morphologies depending on the preparation route. SEM image of Cu$_{gc}$ (Fig. 3.b) shows the surface morphology of highly porous. One can see voids and pores in the Cu$_{gc}$ sample. This observation could be attached to the liberation of a huge quantity of gases through the combustion process due to the decomposition of fuel. SEM of the sample obtained through the co-precipitation methods (Cu$_{co}$), Fig. 3.c exhibits a good homogeneous distribution of nanoparticles as compared to those from the green gel (Cu$_{gg}$), Fig. 3.d, and green hydrolysis (Cu$_{gh}$), Fig. 3.e. Instantaneous nucleation of CuFe$_2$O$_4$ nanoparticles occurs in the course of the co-precipitation process, while the crystal growth, is accelerated further through the sol–gel method. This is attributed to the long time necessary to complete the sol–gel process.

TEM micrographs (Fig. 3B) of the cupper ferrite synthesized by green combustion (Cu$_{gg}$), and co-precipitation methods (Cu$_{co}$) show spherical shapes of the NPS nanocrystalline with an average particle diameter of 12 and 17 nm, respectively. Mixed morphological structures including rectangular and octahedral-shaped particles are visualized by TEM for the samples Cu$_{gc}$, Cu$_{mc}$, and Cu$_{gh}$, Fig. (3b,d,e), with an average particle size of 25, 40, and 45 nm, respectively. The result shows that both the morphology and particle size were mostly controlled by reaction conditions.

3.4. Surface properties

The adsorption isotherm was measured to give useful information on the texturing properties of the prepared samples. The BET data of all samples (Fig. 1S a-e), showed nitrogen isotherms of types (IV) and (V) with different hysteresis loops, which are characteristic for mesoporous materials. The BET surface area of Cu$_{gg}$, Cu$_{co}$, Cu$_{gc}$, Cu$_{mc}$, and Cu$_{gh}$, is found to be 59, 48, 39, 34, and 28 m^2/g, respectively, which goes parallel with decreasing the grain size. The pore size was calculated by the BJH method and found to be 8.1, 7.5, 6.2, 5.4, and 4.4 nm, for Cu$_{gg}$, Cu$_{gc}$, Cu$_{mc}$, Cu$_{co}$, and Cu$_{gh}$, respectively.

3.5. Electrochemical characterizations

Fig. 4A demonstrates the CV cycles of the ferrite samples from − 0.2 to 0.8 V vs. saturated calomel electrode at a scan rate of 10 mV s^{-1}. Each CV curve showed a pair of redox peaks indicating the fast redox and pseudocapacitance behavior of the ferrite samples. The specific capacitance (C$_{sp}$) was computed from the CV curves by applying the following equation.[34]

$$C_{sp} = \left(\int IdV \right)/\nu mV \qquad (1)$$

where *I* is the current (A), *V* is the potential window (Volt), *ν* is the potential scan rate, *m* is the mass (gram) of the ferrite in the electrode. The results obtained are listed in Table 1. Cu$_{gg}$ sample with the highest surface area and pore volume showed the highest capacitance value. Therefore, the CV behavior of this sample at different scan rates was studied (Fig. 4B). It can be seen that with increasing the scan rate, each of the currents and areas under curves increase referring to ideal capacitive behavior.[35] The increase in capacitance with decreasing the scan rate can be attributed to the low diffusion of electrolyte ions. At a lower scan rate, the electrolyte ions have enough time to contact the outer and interior active sites of the ferrite surface leading to
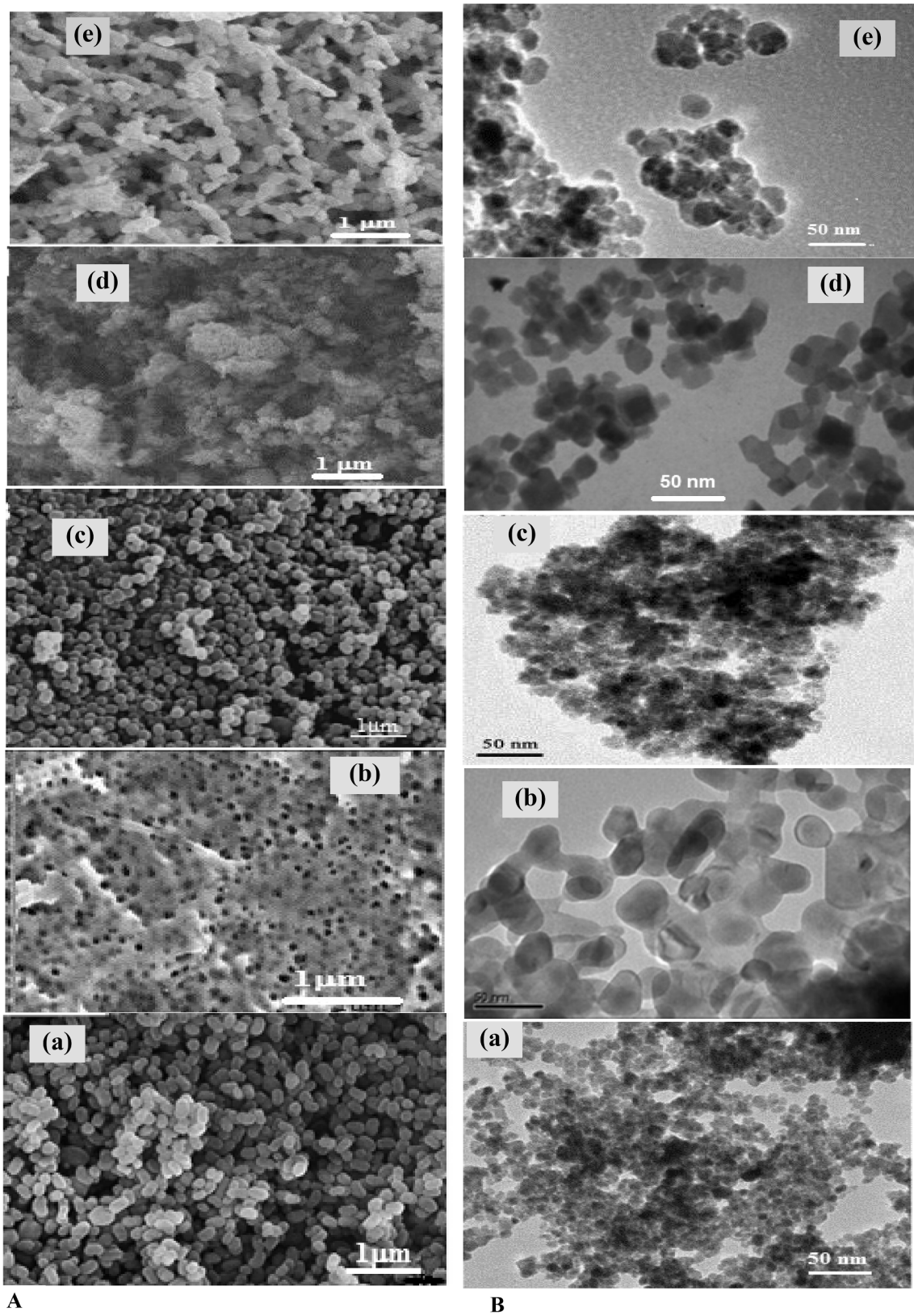
Fig. 3. A) SEM imahges ogf CuFe$_2$O$_4$ samples: (a), Cu$_{mc}$; (b), Cu$_{gc}$; (c), Cu$_{co}$; (d), Cu$_{gg}$ and (e), Cu$_{gh}$. B) TEM images of CuFe$_2$O$_4$samples: (a), Cu$_{gg}$; (b), Cu$_{mc}$; (c), Cu$_{co}$; (d), Cu$_{gh}$ and (e), Cu$_{gc}$.

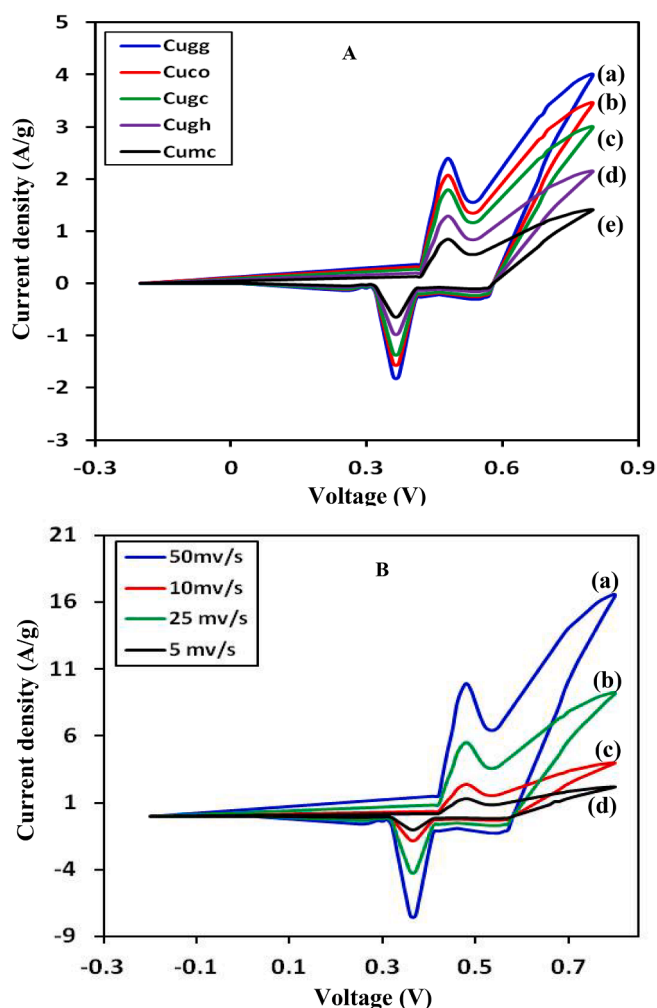**Fig. 4.** A) CV plots for $CuFe_2O_4$ samples in 1 M LiCl at a scan rate 10 mv/s. B) CV plots for Cu_{gg} at the different cycling rates.

accumulating a big number of charges, which is the source of the high specific capacitance value.[36]

The galvanostatic charge/discharge measurements were also used to study the electrochemical performances of $CuFe_2O_4$ electrodes in 1 M LiCl at several current densities between 0.5 and 5 A g^{-1} under a potential window from −0.2 to 0.8 V. Fig. 5.a demonstrates the galvanostatic charge/discharge cycles of ferrite samples measured by applying a current density of 1 A/g. The specific capacitance of the ferrite electrodes was calculated from the discharge curve according to:

$$C_{sp} = I_m \times \Delta t / \Delta V \qquad (2)$$

where I_m is the current density in A g^{-1}, Δt is the discharge time in s, and ΔV is the potential drop during discharge. The results acquired are listed in Table 1 and show good agreement with the CV results, in which the Cu_{egg} sample exhibits the highest specific capacitance. The C_{sp} value of

Cu_{egg} was found to decrease with raising the current density from 0.5 A g^{-1} to 5 A g^{-1}, Fig. 5.b. This may be attributed to the existence of inner active sites, which are unable to participate in redox transitions at high current densities. This implies that some zones of the electrode surfaces are unapproachable at higher current.[37] Fig. 5.c illustrates the dependence of the specific capacitance on current density for Cu_{gg} electrode. Fig. 5.d demonstrates the electrochemical cyclic permanence of Cu_{gg} electrode. For supercapacitor applications, cycling stability is an important parameter. Thus, we studied the durability of Cu_{gg} by the galvanostatic tool using a current density of 1 A/g. The capacitance of the electrode was almost steady up to 1000 cycles, and capacity retention of 90.2% was attained at the 500th cycle, revealing that the Cu_{gg} electrode had respectable recycle-ability for capacitor devices.

The specific capacitance of our Cu_{gg} sample (145F/g) is higher than that of other ferrites obtained at the same scan rate 10 mV/s. B. Saravanakumara, et al. reported C_{sp} value of 127.9F/g for $CuFe_2O_4$ nanoparticles,[38] whereas Bhujun et al. reported C_{sp} values of 103.9, 46.7, and 8.39F/g for $CuFe_2O_4$, $NiCoFe_2O_4$ and $NiCuFe_2O_4$, respectively.[39]

The electrochemical properties of the investigated electrodes were also studied using electrochemical impedance technique (EIS) in the frequency range from 0.01 Hz to 100 kHz with AC bias voltage of 0.01 V. The Nyquist plots are represented in Fig. 6. Each plot comprises a semicircle in the high-frequency region and a straight line in the low-frequency section represents the Warburg impedance. The big differences in the Warburg impedances refer to the large differences in the track distance of the ion diffusion and turn in the resistance of the progress of ions. The catch of the semi-circle with the real axis (Z) at high frequencies represents equivalent series resistance (ESR) which is attributed to several impedance processes: (a) electrode materials intrinsic resistance, (b) LiCl electrolyte ionic resistance, (c) interfacial resistance between the current collector and electrode.[40] The source of the arc at a higher frequency region is attributed to resistance of charge transfer of ions (R_{ct}) at the electrolyte–electrode boundary and is determined by the intersection of the semi-circle with the real axis (Z). [41] Each of ESR and R_{ct} obtained from the Nyquist plots (Fig. 6) is listed in Table 1. The relatively lower value of R_{ct} of Cu_{gg} indicated its better charge transfer ability than other samples. The Warburg angles obtained for all samples are more vertical than 45° referring to the good electrochemical super capacitance. The ferrite electrode shows an increase in vertical inclination according to: $Cu_{gg} > Cu_{co} > Gu_{gp} > Cu_{gh} > Cu_{mc}$. This finding indicates that the Cu_{gg} electrode demonstrates less resistance to ions diffusion, which might be attributed to the short diffusion path of ions, greater surface area, and better electrical conductivity. The Cu_{gg} sample has the greatest BET surface area than other samples. The outstanding current response and large surface area make the Cu_{gg} sample a more consistent electrode for high-performance supercapacitors.

The frequency (f^o), corresponding to the maximum of imaginary impedance (Z") of the semicircle in the EIS, was used to estimate the time constant (τ) of the capacitor according to Eq. (3) [42]

$$\tau = 1/f \qquad (3)$$

From the frequency (f^o, Hz) matching to the maximum of imaginary impedance (Z") of the semicircle in the EIS, the time constant (τ) of the capacitor is estimated using the following equation: $\tau = 1/f^o$.[40] The

Table 1
Surface and electrochemical data for the investigated $CuFe_2O_4$ samples.

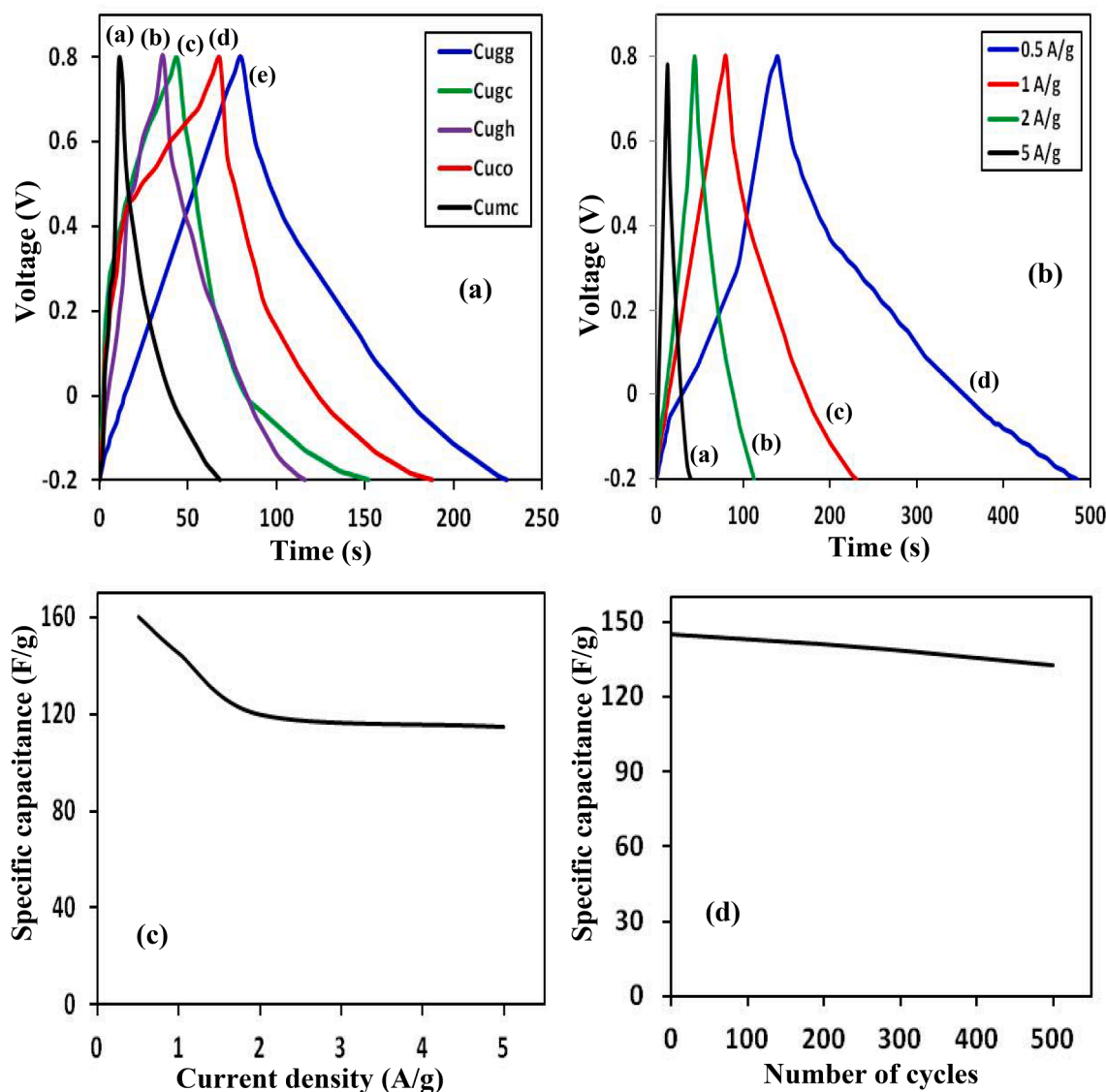| Sample	Particle Size (nm)	$S_{BET}(m^2/g)$	Pore diameter (nm)	C_{sp} (CV)F/g,scan rate10 mv/s	C_{sp}(CD) (F/g),current density (1A/g)	R_{ct}(ohm)	ESR (ohm)	$EWhKg^{-1}$	$PWKg^{-1}$
Cu_{gg}	12	59	8.1	160	145	1.5	7	18.9	486
Cu_{cp}	17	48	5.4	135	116	15.5	27	14.9	487
Cu_{gc}	25	39	7.5	128	104	12	15	13.5	433
Cu_{mc}	40	34	6.2	87	76	13.3	14	9.5	470
Cu_{gh}	45	12	4.4	58	55	11	14	6.8	453

Fig. 5. a) CD plots for the investigated CuFe$_2$O$_4$ samples at a current density of 1 A g^{-1}, b) CG curves for Cu$_{gg}$ sample at different current densities, c) Effect of charging current density on the specific capacitance of Cu$_{gg}$ and d) Effect of the number of cycles on the stability of Cu$_{gg}$ capacitance.

values of τ are found to be 5.1, 9.9, 12.1, 17.8 and 25.7 for Cu$_{gg}$, Cu$_{co}$, Cu$_{gp}$, Cu$_{gh}$, and Cu$_{mc}$, respectively. Low values of τ are ideal for electrochemical capacitors for the rapid charge–discharge processes.[42]

The power density (P) and average energy density (E) of the electrochemical capacitors were determined from Eqs. (4) and (5) [43]

$$E = 0.5\left[1000C_s(\Delta V)^2\right]/3600 \qquad (4)$$

$$P = E \times 3600/\Delta t \qquad (5)$$

where P is the power density (kW kg^{-1}), E is the energy density of the electrode (Wh kg^{-1}), Δt is the time for a sweep segment, Cs is the specific capacitance of the supercapacitor (Fg^{-1}) and ΔV is the voltage change during the discharge process. The results obtained are given in Table (1). The calculated values of E and P for Cu$_{egg}$ sample were analyzed and plotted against each other (Fig. 7) and generally referred to as the Ragone plot. The plot shows almost an ideal knee shaped pattern for the E-P relationship.

4. Conclusions

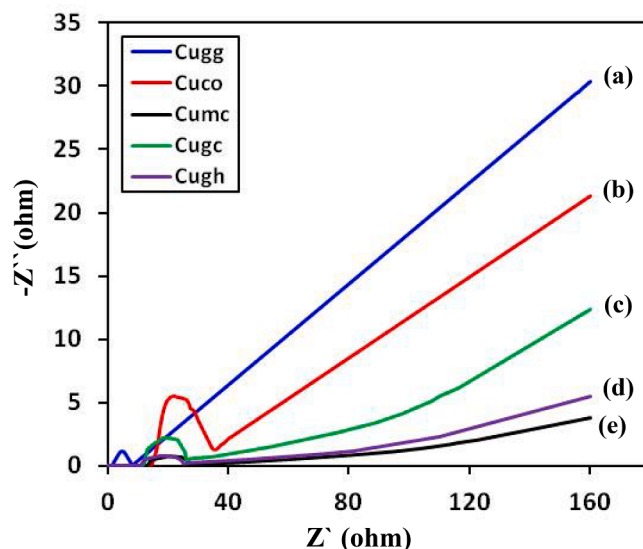To summarize, we have prepared copper ferrite using green and

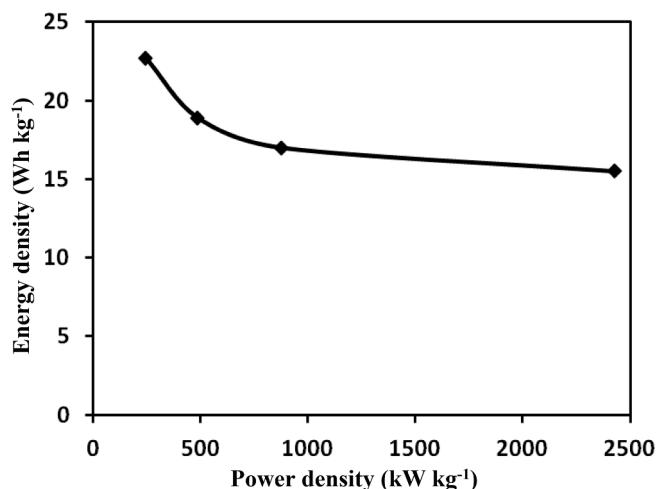**Fig. 6.** Nyquist plots of the investigated CuFe$_2$O$_4$ samples.

Fig. 7. Ragone plot of Cu$_{gg}$ calculated from galvanostatic charge/discharge curves at different current densities.

chemical different synthetic routes. The nanoparticles were characterized by XRD, SEM, FT-IR. XRD patterns show that the main powder phase is the spinel structure. The crystallite size, morphology, textured surface, and electrochemical properties have been largely affected by synthetic tools. The particle size was determined from XRD and TEM data. The crystallite size of the produced copper ferrite powders was in the range between 12 and 45 nm. The BET analysis reveals the presence of a mesoporous structure in these cupper ferrite NPs with a specific surface area varies between 28–59 m^2/g. The CuFe$_2$O$_4$ powders showed different electrochemical properties depending on their particle sizes. The studies revealed that the green sol–gel method was superior to the other methods for producing nanoparticles with smaller crystallite size and highest electrochemical super capacitance efficiency. The Cu$_{gg}$ sample showed a high specific capacitance of approximately 145F/g at a current density of 1 A/g and excellent cycle life of 90.2% after 1000 cycles.

Declaration of Competing Interest

The authors declare that they have no known competing financial interests or personal relationships that could have appeared to influence the work reported in this paper.

Appendix A. Supplementary data

Supplementary data to this article can be found online at https://doi.org/10.1016/j.mseb.2020.114812.

References

[1] M.A. Mousa, M. Khairy, M. Shehab, Nanostructured ferrite/graphene/polyaniline using for supercapacitor to enhance the capacitive behavior, J. Solid State Electrochem. 21 (2017) 995–1005.
[2] T. Tatarchuk, M. Bououdina, J. Judith Vijaya, L. John Kennedy, Nanophysics, Nanomaterials, Interface Studies, and Applications, Springer Proceedings in Physics, Springer International Publishing AG, 2017.
[3] H. El Moussaoui, T. Mahfoud, S. Habouti, K. El Maalam, M. Ben Ali, M. Hamedoun, O. Mounkachi, R. Masrour, E.K. Hlil, A. Benyoussef, Synthesis and magnetic properties of tin spinel ferrites doped manganese, J. Magn. Magn. Mater. 405 (2016) 181–186.
[4] K.K. Kefeni, T. Msagati, B.B. Mamba, Ferrite nanoparticles: synthesis, characterisation and applications in electronic device, Mater. Sci. Eng. B 215 (2017) 37–55.
[5] Y.L. Pang, S. Lim, H.C. Ong, W.T. Chong, Research progress on iron oxide-based magnetic materials: synthesis techniques and photocatalytic applications, Ceram. Inter. 42 (2016) 9–34.
[6] M. Khairy, M.A. Mousa, Influences of γ–Radiation and Surfactants on Electrical and Magnetic Properties of Cu$_{0.1}$Zn$_{0.9}$Mn$_2$O$_4$ Nanoparticles Inter, J. Mater. Chem. 2 (5) (2012) 197–204.
[7] E.E. Ateia, M. Farag, Amelioration of ceramic properties via different preparation techniques, Appl. Phys. A 124 662 (2018) 10 pages.
[8] J. Ding, P.G. McCormick, R. Street, Formation of spinel Mn-ferrite during mechanical alloying, J. Magn. Magn. Mater. 171 (1997) 309–314.
[9] D. Chen, D.-Y. Li, Y.-Z. zhang, Z.-T. Kang, Preparation of magnesium ferrite nanoparticles by ultrasonic wave-assisted aqueous solution ball milling, Ultrason. Sonochem. 20 (2013) 1337–1340.
[10] R. Singh, M. Kumar, L. Tashi, H. Khajuria, H.N. Sheikh, Hydrothermal synthesis of nitrogen doped graphene supported cobalt ferrite (NG@CoFe$_2$O$_4$) as photocatalyst for the methylene blue dye degradation, Nanochem. Res. 3 (2018) 149–159.
[11] D. Chen, Y. Zhang, C. Tu, Preparation of high saturation magnetic MgFe$_2$O$_4$ nanoparticles by microwave-assisted ball milling, Mater. Lett. 82 (2012) 10–12.
[12] H. Saeidian, F. Moradnia, Benign synthesis of N-aryl3, 10-dihydroacridin-1(2H)-one derivatives via ZnO nanoparticle-catalyzed Knoevenagel condensation/intramolecular enamination reaction, Iran. Chem. Commun. 5 (2017) 237–363.
[13] T.S. Fardood, A. Ramazani, S.W. Joo, Sol-gel synthesis and characterization of zinc oxide nanoparticles using black tea extract, J. Appl. Chem. Res. 11 (2017) 8–17.
[14] A. Sutka, G. Mezinskis, Sol-gel auto-combustion synthesis of spinel-type ferrite nanomaterials, Front. Mater. Sci. 6 (2012) 128–141.
[15] Dobrucka, Dluqasweska, Biosynthesis and antibacterial activity of Zno nanoparticles using Trifolium Pratense flower extract, Saudi, J. Biol. Sci. 23 (2016) 517–523.
[16] H. Su, H. Zhang, F. Liu, F. Chun, B. Zhang, X. Chu, H. Huang, W. Deng, B. Gu, H. Zhang, X. Zheng, M. Zhu, W. Yang, High power supercapacitors based on hierarchically porous sheet-like nanocarbons with ionic liquid electrolytes, Chem. Eng. J. 322 (2017) 73–81.
[17] L.J. Xie, J.F. Wu, C.M. Chen, C.M. Zhang, L. Wan, J.L. Wang, Q.Q. Kong, C.X. Lv, K.X. Li, G.H. Sun, A novel asymmetric supercapacitor with an activated carbon cathode and a reduced graphene oxide-cobalt oxide nanocomposite anode, J. Power Sources 242 (2013) 148–156.
[18] H. Zhang, H. Su, F. Liu, B. Zhang, F. Chun, X. Chu, W. He, W. Yang, Flexible supercapacitors with high areal capacitance based on hierarchical carbon tubular nanostructures, J. Power Sources 331 (2016) 120–126.
[19] R. Köferstein, T. Walther, D. Hesse, S.G. Ebbinghaus, Crystallite growth, phase transition, magnetic properties, and sintering behaviour of nano-CuFe$_2$O$_4$ powders prepared by a combustion-like process, J. Solid State Chem. 213 (2014) 57–64.
[20] A.M. Balagurov, I.A. Bobrikov, M.S. Maschenko, D. Sangaa, V.G. Simkin, Structural phase transition in CuFe$_2$O$_4$ spinel, Crystallogr. Rep. 58 (2013) 710–717.
[21] L. Wang, D.C. Bock, J. Li, E.A. Stach, A.C. Marschilok, K.J. Takeuchi, E.S. Takeuchi, Synthesis and Characterization of CuFe$_2$O$_4$ Nano/Submicron Wire-Carbon Nanotube Composites as Binder-free Anodes for Li-Ion Batteries, ACS Appl. Mater. Interfaces 10 (2018) 8770–8785.
[22] S.S. Selimaa, M. Khairy, M.A. Mousa, Comparative studies on the impact of synthesis methods on structural, optical, magnetic and catalytic properties of CuFe$_2$O$_4$", Ceramic Inter. 45 (2019) 6535–6540.
[23] A. Manikandan, M. Durka, S.A. Antony, Hibiscus rosa-sinensis Leaf Extracted Green Methods, Magneto-Optical and Catalytic Properties of Spinel CuFe$_2$O$_4$ Nano- and Microstructures, J. Inorg. Organomet. Polym. 25 (2015) 1019–1031.
[24] R. Naghikhani, C. Nabiyouni, D. Ghanbari, Simple and green synthesis of CuFe$_2$O$_4$–CuO nanocomposite using some natural extracts: photo-degradation and magnetic study of nanoparticles, J. Mater. Sci: Mater. Electronics 29 (2018) 4689–4703.
[25] R. Jalajerdi, D. Ghanbari, Microwave Synthesis and Magnetic Investigation of CuFe$_2$O$_4$ Nanoparticles and Poly Styrene-Carbon Nanotubes Composites, J. Nanostruct. 6 (2016) 278–284.
[26] A.F. Costa, P.M. Pimentel, F.M. Aquino, D.M.A. Melo, M.A.F. Melo, I.M.G. Santo, Gelatin synthesis of CuFe$_2$O$_4$ and CuFeCrO$_4$ ceramic pigments, Mater. Lett. 112 (2013) 58–61.
[27] B. D Cullity, Elements of X-ray diffraction. Ed Addison Wesley, USA (1978).
[28] R.D. Waldron, Inferared spectra of ferrites, Phys. Rev. 99 (1955) 1727–1735.
[29] R.K. Selvan, C.O. Augustin, V. Šepelák, L.J. Berchmans, C. Sanjeeviraja, A. Gedanken, Synthesis and characterization of CuFe$_2$O$_4$/CeO$_2$ nanocomposites, Mater. Chem. Phys. 112 (2008) 373–380.
[30] J. Natsuki, T. Natsuki, Y. Hashimoto, A Review of Silver Nanoparticles: Synthesis Methods, Properties and Applications, Inter. J. Mater. Sci. Appl. 28 (2015) 325–332.
[31] J. Jeevananda1, A. Barhoum, Y.S. Chan, Al. Dufresne, M.K. Danquah, Review on nanoparticles and nanostructured materials: history, sources, toxicity and regulations Beilstein, J. Nanotechnol. 9 (2018) 1050–1074.
[32] N.T.K. Thanh, L.A.W. Green, Functionalisation of nanoparticles for biomedical Applications, Nano Today 5 (2010) 213–230.
[33] L.E. Euliss, J.A. DuPont, St. Gratton, J. DeSimone, Imparting size, shape, and composition control of materials for nanomedicine, Chem. Soc. Rev. 35 (2006) 1095–1104.
[34] D. Han, P. Xu, P.X. Jing, J. Wang, P. Yang, Q. Shen, J. Liu, D. Song, Z. Gao, M. Zhang, Trisodium citrate assisted synthesis of hierarchical NiO nanospheres with improved supercapacitor performance, J. Power Sources 235 (2013) 45–53.
[35] S. Nagamuthu, S. Vijayakumar, G. Muralidharan, Synthesis of Mn$_3$O$_4$/amorphous carbon nanoparticles as electrode material for high performance supercapacitor applications, Energy and Fuels 27 (2013) 3508–3515.
[36] G. Wang, L. Zhang, J. Zhang, A review of electrode materials for electrochemical supercapacitors, Chem. Soc. Rev. 41 (2012) 797–828.
[37] Z.S. Iro, C. Subramani, S.S. Dash, A Brief Review on Electrode Materials for Supercapacitor, Int. J. Electrochem. Sci. 11 (2016) 10628–10643.
[38] B. Saravanakumara, S.P. Ramachandrana, G. Ravia, V. Ganeshb, R.K. Guduruc, R. Yuvakkumara, Electrochemical performances of monodispersed spherical

CuFe$_2$O$_4$, nanoparticles for pseudocapacitive applications, Vacuum 168 (2019), 108798.

[39] B. Bhujun, M.T. Tan, A.S. Shanmugam, Study of mixed ternary transition metal ferrites as potential electrodes for supercapacitor applications, Results Phys. 7 (2017) 345–353.

[40] M.L. Huang, C.D. Gu, X. Ge, X.L. Wang, J.P. Tu, NiO nanoflakes grown on porous graphene frameworks as advanced electrochemical pseudocapacitor materials, J. Power Sources 259 (2014) 98–105.

[41] M. Balasubramaniam, S. Balakumar, Exploration of electrochemical properties of zinc antimonate nanoparticles as supercapacitor electrode material, Mater. Sci. Semicond. Proc 56 (2016) 287–294.

[42] A. Burke, Ultracapacitors: why, how, and where is the technology, J. Power Sources 91 (2000) 17–50.

[43] Z. Fan, J. Yan, T. Wei, L. Zhi, G. Ning, T. Li, F. Wei, Asymmetric supercapacitors based on graphene/MnO$_2$ and activated carbon nanofiber electrodes with high power and energy density, Adv. Funct. Mater. 21 (2011) 2366–2375.